

Defect sizing in guided wave imaging structural health monitoring using convolutional neural networks

Roberto Miorelli^{a,*}, Clément Fisher^a, Andrii Kulakovskiy^{a,b}, Bastien Chapuis^a, Olivier Mesnil^a, Oscar D’Almeida^b

^a Université Paris-Saclay, CEA, List, 91120, Palaiseau, Gif-Sur-Yvette 91191, France

^b Safran Tech, 78114, Magny-Les-Hameaux, France



ARTICLE INFO

Keywords:

Structural health monitoring
Inversion
Deep neural network
Convolutional neural network
Defect sizing
Guided wave imaging

ABSTRACT

This paper proposes an automatic defect localization and sizing procedure for Structural Health Monitoring based on guided waves imaging. The procedure is applied to an aluminum plate equipped with active piezoelectric sensors. The defect localization and sizing strategy is obtained through the use of a convolutional neural network trained exclusively on numerical simulations of guided wave signals and post-processed by the delay and sum imaging algorithm. The paper shows the effectiveness of the proposed approach to invert both synthetic and experimental data.

1. Introduction

Structural Health Monitoring (SHM) identifies the ensemble of non destructive methods and techniques allowing to monitor the health of a structure under test throughout its lifetime with permanent sensors. The SHM paradigm is particularly adapted for inspecting a structure with specific constraints such as accessibility, for continuous diagnosis and prognosis tasks, or on-demand remote maintenance. SHM techniques allow to test very large portions of the structure by using a sparse network of sensors to automate inspections over large areas. The main industrial sectors interested by SHM are the energy and oil&gas industries with pipes monitoring, the aeronautic industry with the monitoring of large structures (fuselage, wings, etc.) as well as the civil engineering industry.

In the context of SHM, a very promising inspection technique consists of considering ultrasound Guided Waves (GWs). Indeed, GWs can propagate in thin structures over long distances with little attenuation. Therefore, the measurement of interactions between specimen inhomogeneities (i.e. void, delamination, corrosion crack, hole etc.) located far away from the sensors is possible. A typical ultrasound GW-SHM inspection scenario consists of a sparse set of piezoelectric sensors attached to the studied structure to generate and measure GWs signals. Most often, time domain GWs signals are post-processed in order to enhance the detection, localization and characterization of defects by

employing qualitative imaging algorithms. Indeed, compared to analysing raw GW signals, working directly with images facilitate the human interpretation and make the analysis much easier. In the literature a broad set of GW Imaging (GWI) algorithms has been developed and studied [1–5].

In this paper, the Delay-And-Sum (DAS) [2] GWI algorithm is used to generate the images associated to the signals measured by the piezoelectric sensor network. The biggest merit of the DAS in the context of this paper is the fact that it provides easily interpreted images with low computational burden, and only requires a limited knowledge on the GW propagation within the structure.

A major challenge in GW-SHM is to automate the diagnostic operations in a reliable fashion. Among the different objectives are automated detection (e.g., healthy vs. damaged structure), classification (e.g., defect(s) type classification) and regressions tasks (e.g., defect(s) sizing). Machine Learning (ML) algorithms such as kernel machines [6] and Deep Neural Network (DNN) [7] have spread recently in various industries to solve tasks such as security and video surveillance, image recognition, natural language interpretation, etc. One of the main advantages of using DNN compared to kernel machines algorithms, consists of the fact that the feature engineering stage can be avoided, which is not the case with kernel-based techniques, largely limiting the deployment of the latter to a narrow spectrum of use cases due to the need of human intervention. Indeed, loosely speaking, a DNN

* Corresponding author.

E-mail address: roberto.miorelli@cea.fr (R. Miorelli).

architecture extracts automatically the most suitable features through the optimization of the architecture's millions or even billions of weights. The drawbacks of such an approach is first that DNN are often seen as black-box object of which the inner operations are difficult to understand and second that it requires relatively large databases for training.

In the framework of Non Destructive Testing (NDT), the use of ML methods has been proposed with good success in eddy current testing [8–11], infrared thermography [12–15], ultrasound testing [16–19,34], or even X-ray [20–22]. Even though the various NDT inspection methods output data of different nature, a ML process can be tailored for each application. Typically, eddy current testing deals with complex valued measurements, X-ray data are represented by gray scale images whereas infrared thermography data is described by real valued time domain signal. The latter is also often used to represent ultrasound signals (i.e., A- and B- scans). The various format of the input data of the ML steps requires a specific care on the selection and tailoring of the specific ML procedure to be used in order to reach satisfying performance. For example, the cardinality (i.e. size of the inputs) of the problem may greatly impact the overall performance in terms of accuracy and efficiency.

In this context, the objective of this paper is to develop a DNN architecture to automatically invert defect position and size based on GWI images generated by simulations. The motivation to use simulations to train the DNN is to limit the cost of database generation, in general much lower in simulation than in experiment. Such approach however requires a thoroughly validated simulation tool within the perimeter of parameters used for the training. The main contributions of this paper are the following.

1. In contrast to many other works in the literature such as [16–19] addressing classification tasks based on ultrasound testing, the regression problem is solved automatically to invert defect size and location. Toward this end, a DNN approach exploiting a Convolutional Neural Network (CNN) architecture specifically developed to deal with GWI data is proposed. For the sake of brevity, this network architecture is referred to as ShmGwi-InvNet.
2. Within the framework of GWI data as CNN input, the interpretability of the per-layer operations of the CNN is discussed in order to shed some light on the inner operations of the CNN architecture under consideration. That is, considering the response of the neurons at different depths (i.e., the feature maps), the pertinence of the features extracted during the training phase are analysed. These indications can be used to interpret and explain the working mechanism associated to the designed network, hence provide input to improve the network architecture and mitigate the “black-box effect”.
3. A third distinguishing point of this contribution resides on the use of synthetic data needed to generate the set of training samples to feed the ShmGwi-InvNet. The inversion performance has been tested on both synthetic (i.e. simulated) and experimental GWI data even though the training is done exclusively on simulated data. This choice requires to develop a robust calibration procedure between simulated and experiment inputs. This last step is especially critical because it demonstrates that a numerically trained neural network can be directly used to invert experimental data and, because large database generation is easier to conduct numerically than experimentally, it greatly widens the potential field of application of such techniques.

The GW-simulations used in this paper are achieved using the SHM module of the CIVA software, which relies on a high order finite element technique [23] to ensure fast computations without simplifying geometries or requiring dedicated computing hardware. Because the simulations aspects are of little importance for this paper, the reader is invited to refer to Ref. [24] for more details. Other simulation processes

could indeed be used as long as two requirements are met: first the match between simulations and experiments must be sufficient and second, simulations must be fast enough to ensure large database generations. Other relevant simulation techniques include boundary element method [25] or GPU-accelerated finite elements [26].

The paper is structured as follows: In Section 2 the studied configuration and the imaging process are presented, along with the calibration procedure. In Section 3 the ShmGwi-InvNet architecture specifically developed for GWI inversion is presented, and is then used to obtain the synthetic and experimental results analysed and discussed in Section 4. In the latter section, some insights on the inner working mechanism associated to DNN architecture developed through the study of features extracted at different layers are also provided. Conclusions, remarks and the ongoing research axes on the application of ML to automatic detection and regression applied to SHM problems are provided in the last section of this paper.

2. SHM guided waves imaging

This section describes the GWI technique employed to post-process ultrasound GWs signals measured by a piezoelectric sensor network attached to the structure of interest. The outcome of the GWI process is image-like signals containing features that can be more easily interpreted by human operators than GWs raw signals in the time domain. Indeed, being multimodal and dispersive, GW raw signals are too complex to be analysed directly by a human operator. Moreover, if P stands for the number of piezoelectric sensors probing the structure, the number of GWs signals to be analysed is equal to $P \times (P - 1)$ raw signals if pulse-echo signals are not recorded. Hence the GWI is an excellent way to combine all the measurements into a single easily interpretable image. The following section provides a brief overview on the delay-and-sum GWI algorithm [2] applied to SHM problems. It is worth mentioning that other kinds of GWIs algorithms such as Rapid, Excitelet or Minimum Variance [1,3,4,27,35] can also be exploited for inversion following the procedure detailed in this paper. However in this work, the DAS algorithm has been chosen since it provides a good trade-off between robustness, implementation simplicity and computational efficiency.

2.1. The delay and sum algorithm applied to SHM

The SHM configuration under study is shown in Fig. 1. It is an aluminum panel instrumented with 8 circular piezoelectric transducers. The DAS algorithm can be formulated as follows: Let us consider an SHM system composed of P piezoelectric sensors with a round-robin scanning procedure, i.e. each transducer sequentially generates an ultrasonic pulse while the other $P - 1$ remaining sensors measure the propagated

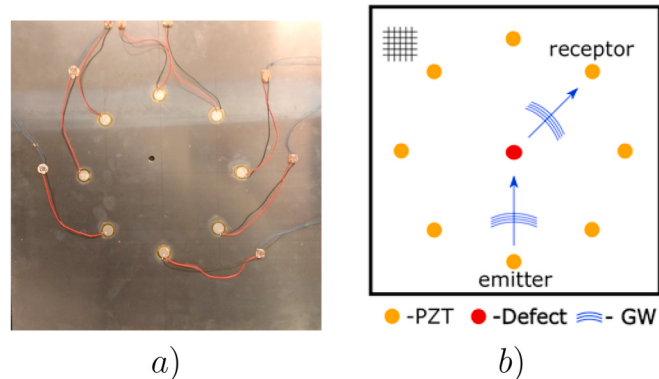


Fig. 1. SHM experimental setup with in a) the aluminium plate with eight piezoelectric sensors encircling area to monitor damaged by a through-hole and b) a sketch of the experimental measurement procedure.

wavepackets. Subsequently, a discrete 2D-grid is defined over the whole area of interest. An arbitrary grid point is identified by its coordinates (x, y) to which is associated a Damage Index (DI) given as

$$\text{DI}(x, y) = \sum_{k=1}^{P(P-1)} r^k(\tau^k(x, y)) \quad (1)$$

where $r^k(\cdot)$ is the envelope of the residual signal of the k -pair of sensors, defined as the difference between the signal in the pristine state and the signal in the damage state, and $\tau^k(x, y)$ represents the GWs theoretical time of flight associated to the inspection point (x, y) for the transmission receiver path numbered k . The theoretical time of flight $\tau^k(x, y)$ is computed assuming no dispersion by:

$$\tau^k(x, y) = \tau(x, x_i, x_j; y, y_i, y_j) = \frac{1}{C_g} \left[\sqrt{(x - x_i)^2 + (y - y_i)^2} + \sqrt{(x - x_j)^2 + (y - y_j)^2} \right] \quad (2)$$

in Eq. (2), the subscripts i and j identify the positions associated to the emitting and receiving PZT sensors corresponding to the path of index k , respectively. C_g stands for the group velocity associate to the path going from the i -th transmitter to the j -th receiver passing through the inspection point located at (x, y) . Typically such a value can be either inferred by simulations or measured. Note that in DAS, C_g is constant, i.e. the dispersion effect are neglected, which is a reasonable assumption as long as the excitation pulse is narrow-band. Note that for anisotropic propagation media such as composites, C_g is a function of the propagation direction. The envelope of the residual signal in (1), is computed as $r(t) = \sqrt{s_r(t)^2 + \hat{H}(s_r^k(t))^2}$ where $\hat{H}(s_r^k(t))^2$ refers to the Hilbert transform and

$$s_r(t) = s_c(t) - s_b(t) \quad (3)$$

is the residual signal calculated by subtracting the current state signal $s_c(t)$ from the pristine baseline signal $s_b(t)$. Note that the DAS process is similar to the SAFT (Synthetic Aperture Focussing Technique) [28] with the following two differences. First, in DAS the baseline signals are used (Eq (3)) to better highlight the signature of the defect and be more robust to additional effects, such as edge reflections. Second, in SAFT, a unique line of sensors is often used to image the structure, assumed to be unidirectional in the direction orthogonal to the sensor line while in DAS the monitored structure is often surrounded by sensors to ensure multidirectional inspection and have a better chance to monitor directive defects such as cracks.

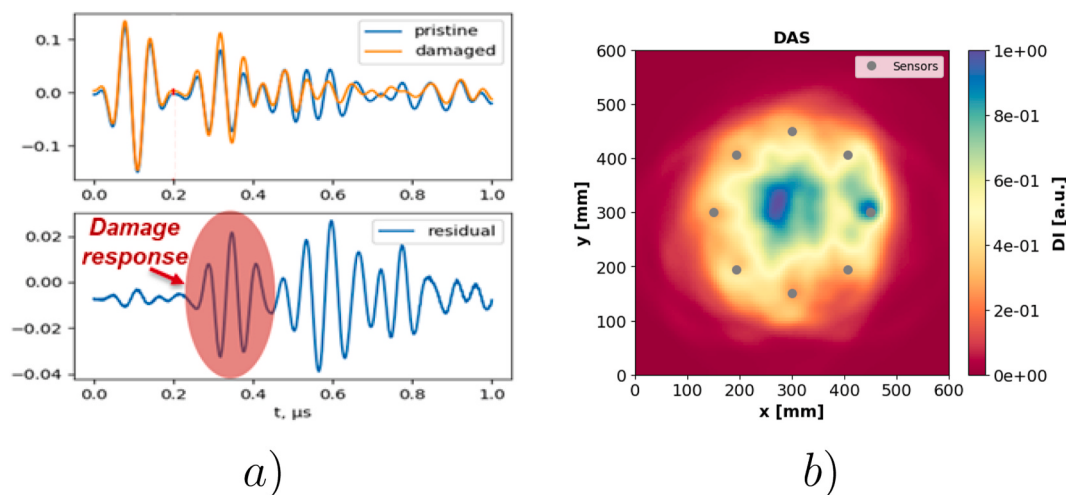


Fig. 2. An example of experimental GWs signals leading to a DAS image with a) raw signal (top) and residual signal (bottom) for an emitting-receiving couple with a 40 kHz 2-cycle tone burst and b) The resulting DAS image; the piezoelectric sensors are represented by the black dots and the colormap is the Damage Index.

The application of the DAS imaging process is illustrated in Fig. 2: first, an example of pristine (blue) and damaged (orange) signals are shown at the top of Fig. 2a. The corresponding residual signal (i.e. the difference) is shown just below. For clarity purposes, the incident wavepacket from the damage is highlighted in red, the subsequent wavepackets being the reflections on the edges of the plate. Note that a single signal path is represented here while a total of $P \times (P - 1) = 56$ such signals are used for imaging. In Fig. 2b is shown the DAS image computed by the previously described process. In this result, a high pixel intensity is represented by the blue color and highlights a high damage index. Straightforward interpretation of GWI can be a difficult task and human-error are possible due to the presence of false alarms (as can be seen in Fig. 2b) on the zone close to the central-right sensor). The use of the machine learning strategy presented in this paper aims to mitigate this issue.

3. Model-driven supervised learning based on GWI data

In this section, the details about the model-driven methodology developed in this paper to design the CNN architecture for defect sizing based on DAS images are presented. First some details about the generation of the datasets required for training, validation and testing are provided. The datasets are based on synthetic GWI images generated through the CIVA software [23,24]. Subsequently, the CNN architecture is developed, detailing the various layers.

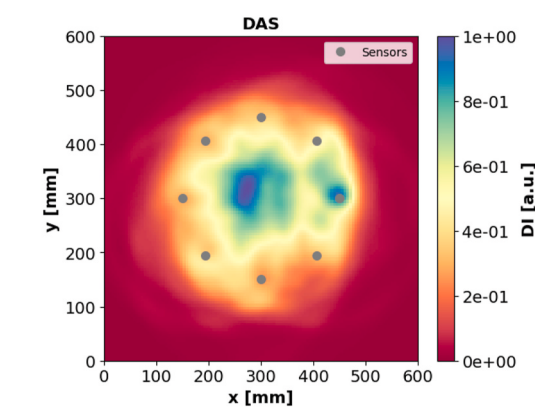
3.1. Deep learning inversion strategy based on convolutional neural networks

In NDT and SHM, the availability of experimental labelled data may be limited and does not allow to effectively train machine learning algorithms. Note that for SHM, the limited data availability problem might be solved for specific use-cases in which sensor deployment and data collection over time has been achieved, but the collected data will remain use-case specific and are unlikely to be directly useful for other applications. To overcome this issue, synthetic data is generated by the SHM module of the CIVA software [23]. The software provides the possibility to simulate GWs signals and subsequently post-process them by using the DAS algorithm.

A dataset is defined as a collection of input-output couples as

$$D = \{(\mathbf{X}_1, \mathbf{y}_1), \dots, (\mathbf{X}_N, \mathbf{y}_N)\} \subseteq (\mathbf{X} \times \mathbf{Y})^N, \quad (4)$$

With N stands for the number of samples contained in the dataset. \mathbf{X}_i is a matrix containing the i -th GWI image such that $\mathbf{X}_i \in \mathbb{R}^{Nx \times Ny}$ with Nx



and N_y representing the number of pixels used to discretize the image along the x and y directions, respectively. $\mathbf{y}_i \in \mathbb{R}^{N_p}$ is the vector of N_p entries associated to the flaw parameters used to simulate the i -th DAS image, i.e. the flaw size and position. In other words, the supervised learning strategy employed in this paper aims at mapping the space of the GWI post-processed signals (i.e., the features represented by the GWI) to the space of flaws parameters. This approach is schematized in Fig. 3. In the next section, the details about the CNN architecture developed to effectively carry out this mapping are presented.

3.2. The ShmGwi-InvNet architecture

In the following, more insights about the CNN employed to map the GWI data on the model parameter space block labelled “ShmGwi-InvNet” illustrated in Fig. 3 are provided. In this work, due to the cardinality of the addressed problem (i.e., each image has $N_x \times N_y$ pixels), a deep learning approach based on multi-layer perceptron (MLP) easily turns to be a computationally demanding task. Indeed, a typical GWI image is made of around $N_x \times N_y = 100 \times 100 = 10^4$ pixels. As a consequence, the number of hidden units (i.e., the neurons) and the number of hidden layers cannot be increased without a heavy impact on the number of parameters to be estimated [29]. Besides the obvious increase in terms of computational time, the second drawback consists of the fact that having more parameters to tune requires more training data to avoid overfitting. Thus, the training set generation turns to be very costly and computationally expensive. A widely employed approach to tackle this problem consists of adopting a CNN-based deep learning paradigm. Compared to MLP, CNN architectures enable sparse interaction by employing convolutional kernels, sharing the weights through different layers hence limiting the number of parameters to be estimated [7]. Furthermore, CNN naturally allow to work with 2D-images without having to go through the vectorization of matrices that may break down the spatial coherence of images leading, for certain cases, to a more difficult learning procedure.

The ShmGwi-InvNet network architecture is represented in Fig. 4a) and can be described as follows. The ShmGwi-InvNet is composed of an input layer of size $N_x \times N_y$, i.e. the size of the GWIs, followed by three convolutional layers, two fully-connected MLP layers and an output layer. Each of the convolutional blocks is composed of the concatenation of elementary tasks performing convolution, activation function, and max-pooling operations as sketched in Fig. 4b). The k -th convolutional layer takes as input a matrix of size $N_x^{(k)} \times N_y^{(k)}$ (where, with $k = 1$, $N_x^{(1)} \times N_y^{(1)} = N_x \times N_y$) and applies on convolutional $F^{(k)}$ filters with size $(F_x^{(k)}, F_y^{(k)}) = (3, 3)$ with zero-padding and a stride equal to one. In the activation layers, the computed filter responses pass through the Rectified Linear Unit (ReLU) activation function $f_{ReLU}(\mathbf{z}) = \max(0, \mathbf{z})$. Subsequently, the output passes through the pooling layer operating independently on each of the activation maps by performing a maxpooling

operation based on a filter of size $(P_x^{(k)}, P_y^{(k)}) = (2, 2)$ aiming at reducing the image size by a factor of four. These operations are repeated two times, where 64 and 128 feature maps have been chosen for the first and the second convolutional block, respectively. Thus the obtained feature maps are vectorized and connected to two layers of fully-connected neural network made of 128 and 32 neurons, respectively, and activated by the ReLU function. The last fully connected layer is the output layer composed of N_p output neurons. The weights optimization has been carried out by using Adam optimization algorithm. The architecture was implemented by using the Python library Tensorflow [30].

4. Numerical and experimental validation

In order to assess the performance of the ShmGwi-InvNet numerical and experimental validations are performed based on a set of simulations and measurements carried out at CEA-List laboratories. The details about the experimental setup employed and the details associated to the dataset used for training, validation and test purposes generated via CIVA are provided in the next sub-sections.

4.1. Experimental setup description, calibration procedure and dataset generation details

The SHM inspection problem under consideration in this work is shown in Fig. 1. An aluminum panel of dimension $600 \times 600 \times 3$ mm has been equipped with eight 18 mm diameter piezoelectric sensors sequentially emitting a 2-cycle burst of central frequency equal to 40 kHz equally spaced on the circumference of a 300 mm diameter circle. The 2-cycle excitation was used to ensure a sufficient spatial resolution of the imaging for sharp defect imaging. The excitation frequency is chosen relatively low as the resulting wavelength is sufficient to image the smallest defect under consideration. A round robin acquisition procedure has been performed with all the PZT sensors, as shown in figure Fig. 1b), afterwards the acquired signals have been post-processed via the DAS algorithm. At this frequency, the dominant mode is the A0 mode with a wavelength of 25 mm. In order to introduce a controlled defect in the plate at the coordinates $p_x = 250$ mm and $p_y = 320$ mm, a through-hole has been drilled with increasing radius, i.e., $r = [2.5, 3.0, 3.5, 4.0, 4.5, 5.0, 5.5, 6.0, 7.5]$ mm, at a fixed location (see Fig. 1a)). This experiment provides a single defect position with 8 defects sizes and will be used to validate the numerically-trained regression model. This experimental data is not used in the learning or validation procedure of the CNN. It is worth mentioning that the patterns contained within the GWIs depends on both defect location and size. As a consequence, even though the training set may contain defects sizes close to the experimental one, the GWIs maps behave very differently, as one can notice in Fig. 5. The simulated replica of the experimental configuration (i.e. same defect size and position) is not part of the simulated databases.

To generate the dataset needed for training, validation and test

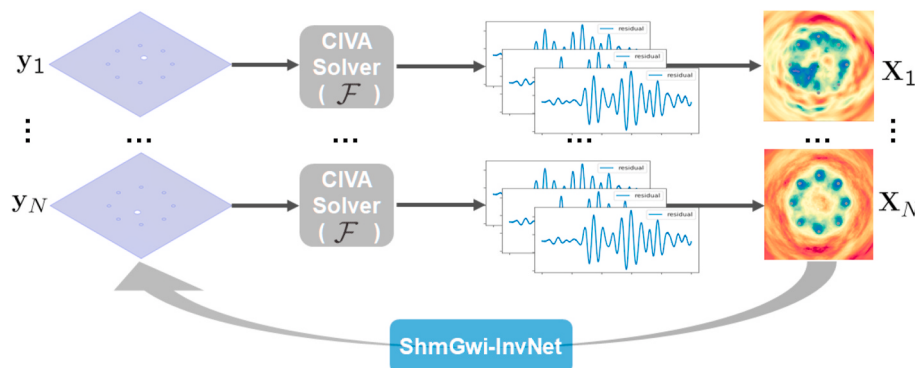


Fig. 3. Proposed model-driven inversion scheme based on CIVA.

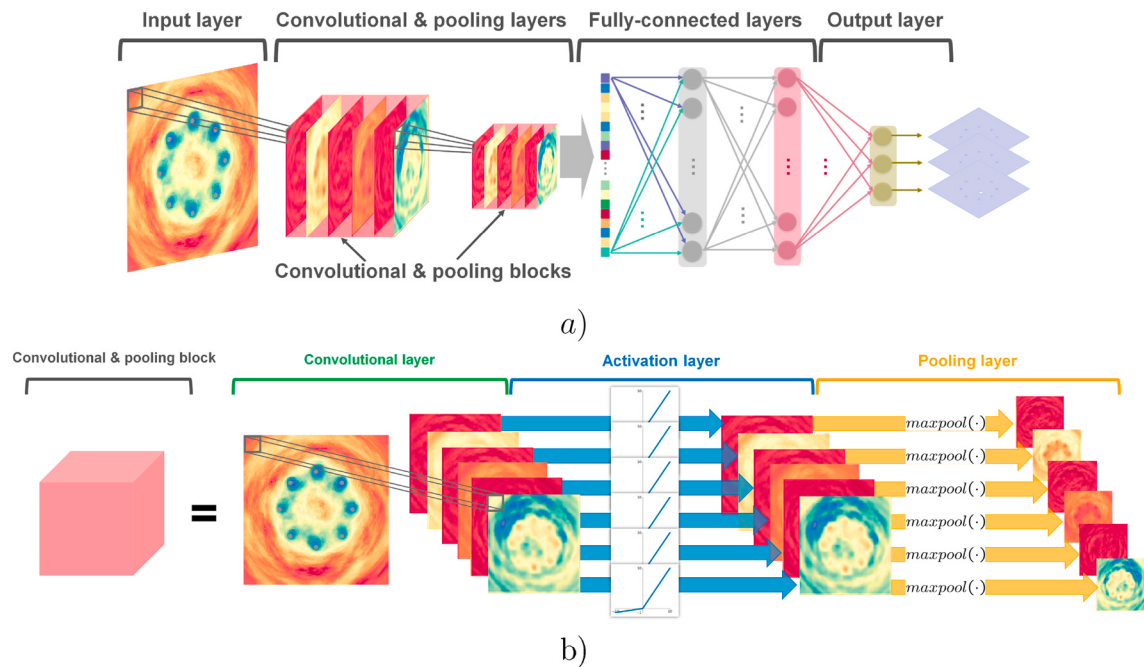


Fig. 4. The ShmGwi-InvNet architecture is shown in a) from input to output layers. In b) a unitary convolutional block architecture is represented.

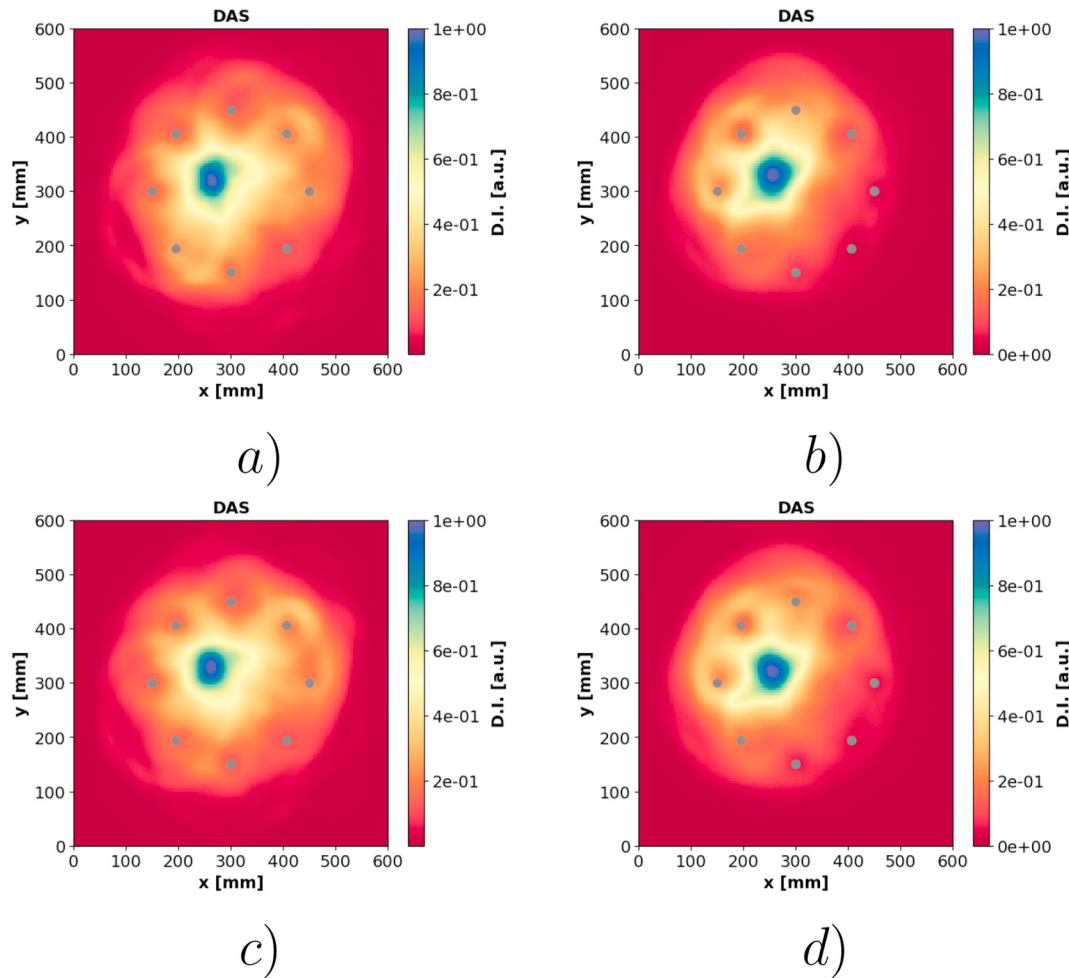


Fig. 5. Normalized GWI obtained via DAS post processing. In a) and c), the experimental maps for two defects having radius equal to 4.5 mm and 6.0 mm, respectively. In b) and d), the simulated maps associated to the experimental test samples in a) and c), respectively.

through CIVA, a three dimensions Latin Hypercube Sampling (LHS) design composed of 500 samples has been created. The variation range of the LHS dataset obtained for x and y positions varies between $p_x = [200.16, 397.34]$ mm and $p_y = [201.6, 398.23]$ mm, respectively whereas the defect radius varies between $r = [2.51, 7.47]$ mm. Subsequently, each configuration is calculated with CIVA and the simulated signals are processed with the DAS algorithm in the same manner as the experimental data, in order to create 500 images each with 120×120 pixels. To train the ShmGwi-InvNet, a subset of $N = 350$ simulated samples are used for training and 10 samples for validation purposes. The remaining 140 samples are used as a synthetic test set to assess the performance of the algorithm on synthetic data.

The absolute amplitude of the signals measured experimentally is a function of several parameters not taken into account in the simulations (e.g., voltage amplification, piezoelectric transduction, etc.). However, besides the absolute amplitude, it is assumed that the experimental and simulated signals are directly comparable. Therefore, a calibration stage is employed to have experimental and simulation signals on the same amplitude scale. The choice is made to modify the amplitude of the raw simulated signals and not to modify the experimental signals. The process is the following. For each transducer path in the pristine state, the ratio between the maximal amplitude of the experimental signal and the simulated signal is computed. Then, for both damage and pristine states and for all the transducer pairs, this ratio multiplies the simulated signals to create the calibrated simulated signals. DAS images are then created from the experimental signals and the calibrated simulated signals. The numerically and experimental DAS images are then directly comparable, the difference between the two being limited to the phenomena not described in the simulations and assumed to be negligible (measurement noise, error in the finite element model convergence, attenuation etc.).

For the subsequent approach to work, the match between experimental and calibrated simulation signals must be excellent. This assumption has been verified by the authors in previous work in a very similar configuration [23].

4.2. ShmGwi-InvNet inversion results

In this section, regression results aiming at retrieving defect positions and defect sizes from both synthetic and experimental tests sets are presented. As a reminder, the CNN is exclusively trained with the calibrated numerical DAS images, then used to invert both numerical and experimental data, without any modification. In Fig. 6, predictions obtained by the ShmGwi-InvNet are provided in terms of true versus predicted values, respectively represented by blue circles and red crosses for the simulated and experimental data. The predictions on experimental data are overlapped to the simulated one to compare the variance of the inversion. As one can notice, in the case of simulated data, the scattered

points are aligned on the diagonal solid line that indicates the best possible agreement between predictions and ground truth. The predictions associated to the experimental data show that the estimation of defect positions is slightly more spread than the synthetic counterpart. Furthermore, defect radius characterization based on experimental data is successful as well and is as spread as the simulated points. In other word, no significant error is induced in the inversion of experimental data compared to the inversion of simulated data. Concerning the experimental test set, it is worth mentioning that the predictions with the two largest errors are the ones associated to values on the training set boundaries (i.e. defect radius equals to 2.5 mm and 7.5 mm). This values are most “critical” due to the absence of a sufficient number of proxy training samples due to the chosen parameters’ variation range.

Quantitatively, the accuracy of the predictions can be quantified by using the Mean Absolute Error $MAE = \sum_{i=1}^T |y_i - \hat{y}_i|/T$, the Root Mean Squared Error $RMSE = \sqrt{\sum_{i=1}^T (y_i - \hat{y}_i)^2}/T$ and through the correlation coefficient defined as $R^2 = 1 - \sum_{i=1}^T (y_i - \hat{y}_i)^2 / \sum_{i=1}^T (y_i - \bar{y})^2$. Where, for each defect parameter, y_i , \hat{y}_i and \bar{y} represents the i -th actual parameter, the predicted one and the mean value of the test set, respectively and T is the test set size. In Table 1 the computed errors based on the entire testing set are provided. In Fig. 7, the prediction error analysis are represented in terms of kernel density estimation computed for each parameter at different defect radius. The analysis of these plots shows that the two localization parameters are almost independent of the flaw radius and the absolute error lesser than 10 mm regardless of whether the horizontal and vertical positions is considered. Concerning the radius estimation, the absolute error is less than 0.5 mm and is completely independent on the flaw radius size. Compared to the A0 interrogating wavelength at 40 kHz of 25 mm, these performance can be judged as excellent.

From a computational standpoint, the ShmGwi-InvNet has been trained in 1200 epochs achieved by early stop criteria. The training phase takes about 20 min to optimize the ~ 15 millions parameters whereas the test time required about 15 msec for the entire 140 test samples. These computational results have been obtained by training and testing the network via GPU on a Dell Precision 5520 Intel Xeon E3

Table 1
Prediction errors associated to the synthetic and experimental test sets.

	MAE [mm]		RMSE [mm]		R^2 [a.u.]	
	Sim.	Exp.	Sim.	Exp.	Sim.	Exp.
x-pos. (p_x)	3.72	21.53	4.43	9.9	0.14	0.36
y-pos. (p_y)	5.03	23.67	5.85	11.21	0.18	0.45
Hole rad. (r)	0.98	–	0.98	–	0.98	0.91

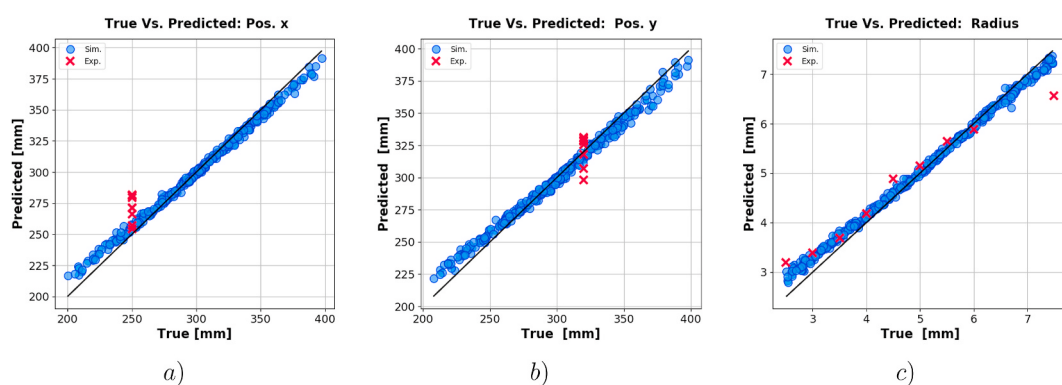


Fig. 6. ShmGwi-InvNet regression results obtained for the following parameter of the defect: a) x-position, b) y-position and c) radius where “●” indicates a prediction based on synthetic data whereas “×” stands for a prediction based on experimental data.

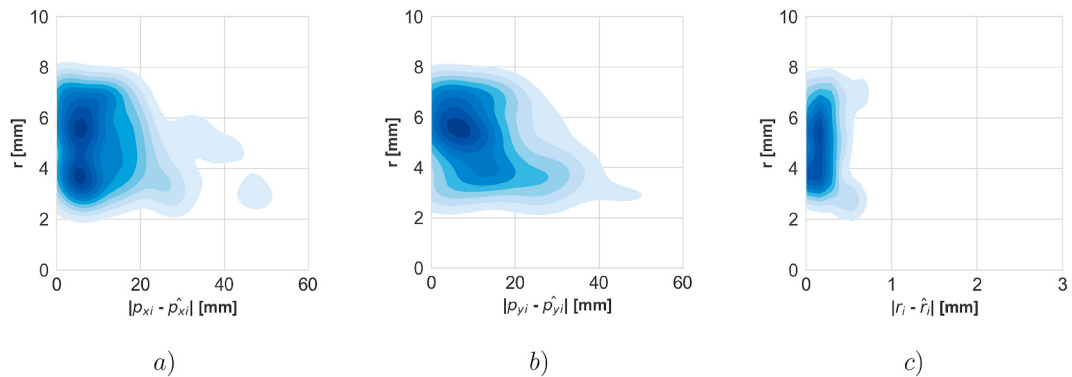


Fig. 7. Kernel density estimation of the absolute prediction errors for different defect radius values. The x -position, y -position and radius are given in a), b) and c), respectively.

– 1505 M processor with 32 GB of RAM and equipped of a Nvidia Quadro M1200 with 4 GB of RAM.

4.3. Analysis of the hidden layers of the CNN

Deep learning algorithms like CNN are often considered as black-box algorithms. Indeed, the inner working mechanisms of a CNN are often difficult to interpret and understand. Very recently the ML community focused a part of its researches to provide more understanding on interpretability and explainability of neural networks [31–33]. Hereafter some elements of interpretation of the CNN are provided by considering the visualization of the neurons activation levels for feature maps at the end of each convolutional block (i.e., after the max pooling). The shallowest layers features maps represent the set of the extracted features closer to the input signals whereas the deepest network layers encode the most abstract features extracted by the CNN. For this analysis, the feature extraction mechanisms associated to the second and the fourth layers of the ShmGwi-InvNet are represented in Fig. 8. These two layers preserve some degrees of interpretability (i.e. the defect position can be easily seen in some neurons), thus they can be used to underline

the feature extraction mechanisms of the ShmGwi-InvNet. Looking at Fig. 8a one can notice that, in the second convolutional block (i.e., after the max pooling), the neurons are activated on the whole map by skipping (i.e., low activation values) the zone nearby the sensors which tends to be set to zero in the convolutional layer 4. Hence it can be concluded that the pixel near the sensors contribute very little to the final predictions. In Fig. 8b), the architecture is able to propagate from the layer 2 to 4 most of the features associated to the presence of the defect located almost in the middle of the plate. That is, the neurons in the layers activate at the spatial location associated to the defect. Furthermore, looking at the feature maps for both the considered images, one can notice that the most active neurons for the feature maps in Fig. 8a) are the less active in Fig. 8b). Such information shows how the CNN has learnt during the training phase by optimizing the network weights.

5. Conclusion and perspectives

In this paper, an inversion strategy based on a deep convolutional neural network is presented. The approach relies on a model-driven

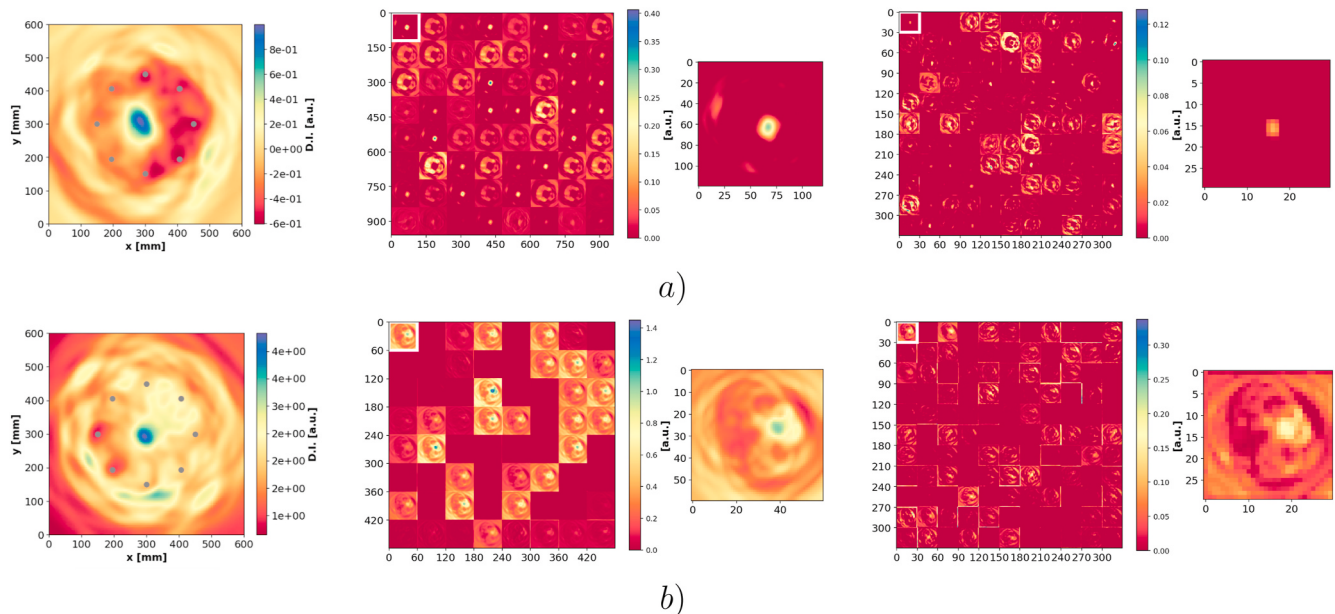


Fig. 8. Analysis of the ShmGwi-InvNet feature extraction procedure for two GWI maps: a) from left to right: GWI image parameterized by $(p_x, p_y, d) = (282.8, 293.5, 5.97)$ mm, the response of the neurons after activation of the second CNN layer with a zoom on the neuron highlighted in white and the response of the neurons after activation of the fourth CNN layer with a zoom on the neuron highlighted in white and b) the same representation for a GWI parameterized by $(p_x, p_y, d) = (304.8, 304.5, 7.06)$ mm.

inversion where simulations conducted with CIVA have been used to train the CNN model. The performance of the proposed CNN architecture are assessed on both simulated and experimental data after training on exclusively simulated data. On both the datasets, successful inversion of defect position and size is conducted, with an average localization error of 10 mm and a sizing error or 0.5 mm, with an interrogating wavelength of 25 mm. Moreover, the experimental predictions present good correlation with the simulated one. This agreement shows that the model-driven approach can be successfully employed to train a robust ML inversion model against unseen experimental and synthetic samples based on GWIs, and quantify features with an accuracy far below the wavelength. Note that this conclusion hold only as long as the simulated data matches reasonably well the experimental data. Furthermore, some insights on the interpretation of the features extracted by the CNN and its inner working mechanisms were presented.

The possible extensions of this works are multiple. The main topic of interest is studying and possibly enhance the capability of the ShmGwi-InvNet architecture on more challenging problems such as the case of multiple-defects problem or to address other kind of defect shape and/or topology. Moreover, the extension and the validation of the proposed model-driven approach to more challenging propagation phenomena as the GW signal in composite materials is also targeted.

On the long term, such approach could be very useful to conduct an automatic diagnostic of GW signals on a structure in which experiments cannot be easily conducted (either for cost or practical reasons). To reach such applications however, exhaustive validation of models would be required to ensure that simulations provide realistic results, including in varying environments.

CRediT authorship contribution statement

Roberto Miorelli: Wrote - original draft, Wrote - review & editing, Design and Perform Research, Investigation.Clément Fisher: Data creation, Investigation, Software.Andrii Kulakovskiy: Data creation, Investigation.Bastien Chapuis: Project administration, Funding acquisition, Resources.Olivier Mesnil: Wrote - original draft, Wrote - review & editing, Data creation, Supervision, Investigation.Oscar D'Almeida: Project administration, Funding acquisition, Resources.

Declaration of competing interest

The authors declare that they have no known competing financial interests or personal relationships that could have appeared to influence the work reported in this paper.

References

- [1] Zhao X, Qian T, Mei G, Kwan C, Zane R, Walsh C, Paing T, Popovic Z. Active health monitoring of an aircraft wing with an embedded piezoelectric sensor/actuator network: ii. wireless approaches. *Smart Mater Struct* 2007;16(4):1218.
- [2] Michaels JE. Detection, localization and characterization of damage in plates with an *in situ* array of spatially distributed ultrasonic sensors. *Smart Mater Struct* 2008; 17(3):035035.
- [3] Quaeghebeur N, Ostiguy P, Masson P. Correlation-based imaging technique for fatigue monitoring of riveted lap-joint structure. *Smart Mater Struct* 2014;23(5): 055007.
- [4] Hall JS, Fromme P, Michaels JE. Guided wave damage characterization via minimum variance imaging with a distributed array of ultrasonic sensors. *J Nondestr Eval* 2014;33(3):299–308.
- [5] Zou F, Rao J, Aliabadi MH. Highly accurate online characterisation of cracks in plate-like structures. *NDT E Int* 2018;94:1–12.
- [6] Scholkopf B, Smola AJ. Learning with kernels: support vector machines, regularization, optimization, and beyond. MIT press; 2001.
- [7] Goodfellow I, Bengio Y, Courville A. Deep learning. MIT press; 2016.
- [8] Ahmed S, Salucci M, Miorelli R, Anselmi N, Oliveri G, Calmon P, Reboud C, Massa A. Real time groove characterization combining partial least squares and svr strategies: application to eddy current testing. In: *Journal of physics: conference series*, vol. 904. IOP Publishing; 2017, 012017.
- [9] Ahmed S, Reboud C, Lhuillier P-E, Calmon P, Miorelli R. An adaptive sampling strategy for quasi real time crack characterization on eddy current testing signals. *NDT E Int* 2019;103:154–65.
- [10] Salucci M, Anselmi N, Oliveri G, Rocca P, Ahmed S, Calmon P, Miorelli R, Reboud C, Massa A. A nonlinear kernel-based adaptive learning-by-examples method for robust ndt/nde of conductive tubes. *J Electromagn Waves Appl* 2019; 33(6):669–96.
- [11] Zhu P, Cheng Y, Banerjee P, Tamburrino A, Deng Y. A novel machine learning model for eddy current testing with uncertainty. *NDT E Int* 2019;101:104–12.
- [12] Lu P, Gao B, Woo WL, Li X, Tian GY. Automatic relevance determination of adaptive variational bayes sparse decomposition for micro-cracks detection in thermal sensing. *IEEE Sensor J* 2017;17(16):5220–30.
- [13] Luo Q, Gao B, Woo WL, Yang Y. Temporal and spatial deep learning network for infrared thermal defect detection. *NDT E Int* 2019;108:102164.
- [14] Duan Y, Liu S, Hu C, Hu J, Zhang H, Yan Y, Tao N, Zhang C, Maldaque X, Fang Q, et al. Automated defect classification in infrared thermography based on a neural network. *NDT E Int* 2019;107:102147.
- [15] Hu C, Duan Y, Liu S, Yan Y, Tao N, Osman A, Ibarra-Castanedo C, Sfarra S, Chen D, Zhang C. Lstm-rnn-based defect classification in honeycomb structures using infrared thermography. *Infrared Phys Technol* 2019;102:103032.
- [16] Ye J, Ito S, Toyama N. Computerized ultrasonic imaging inspection: from shallow to deep learning. *Sensors* 2018;18(11):3820.
- [17] Almansouri H, Venkatakrishnan SV, Buzzard GT, Bouman CA, Santos-Villalobos H. Deep neural networks for non-linear model-based ultrasound reconstruction. In: *2018 IEEE global conference on signal and information processing (GlobalSIP)*, IEEE; 2018. p. 6–10.
- [18] Munir N, Kim H-J, Park J, Song S-J, Kang S-S. Convolutional neural network for ultrasonic weldment flaw classification in noisy conditions. *Ultrasonics* 2019;94: 74–81.
- [19] Posilović L, Medak D, Subasić M, Petković T, Budimir M, Lončarić S. Flaw detection from ultrasonic images using yolo and ssd. In: *2019 11th international symposium on image and signal processing and analysis (ISPA)*, IEEE; 2019. p. 163–8.
- [20] Lin J, Yao Y, Ma L, Wang Y. Detection of a casting defect tracked by deep convolution neural network. *Int J Adv Manuf Technol* 2018;97(1–4):573–81.
- [21] Zhu Q, Ai X. The defect detection algorithm for tire x-ray images based on deep learning. In: *2018 IEEE 3rd international conference on image, vision and computing (ICIVC)*, IEEE; 2018. p. 138–42.
- [22] Mery D. Aluminum casting inspection using deep learning: a method based on convolutional neural networks. *J Nondestr Eval* 2020;39(1):12.
- [23] Mesnil O, Imperiale A, Demaldent E, Chapuis B. Validation of spectral finite element simulation tools dedicated to guided wave based structure health monitoring. In: *American institute of physics conference series*. vol. 2102; 2019.
- [24] Imperiale A, Demaldent E. A macro-element strategy based upon spectral finite elements and mortar elements for transient wave propagation modeling. application to ultrasonic testing of laminate composite materials. *Int J Numer Methods Eng* 2019;119(10):964–90.
- [25] Li J, Khodaei ZS, Aliabadi M. Boundary element modelling of ultrasonic lamb waves for structural health monitoring. *Smart Mater Struct* 2020;29(10):105030.
- [26] Shen Y, Cesnik CE. Hybrid local fem/global lisa modeling of damped guided wave propagation in complex composite structures. *Smart Mater Struct* 2016;25(9): 095021.
- [27] Kulakovskiy A, Chapuis B, Mesnil O, Bedreddine N-R, D almeida O, Lhemery A. Defect imaging on cfrp and honeycomb composite structures by guided waves generated and detected by a sparse pzt array. *Structural Health Monitoring*; 2017 [shm].
- [28] Sicard R, Chahbaz A, Goyette J. Guided lamb waves and l-saft processing technique for enhanced detection and imaging of corrosion defects in plates with small depth-to wavelength ratio. *IEEE Trans Ultrason Ferroelectrics Freq Contr* 2004;51(10): 1287–97.
- [29] Safran I, Shamir O. Depth-width tradeoffs in approximating natural functions with neural networks. In: *Proceedings of the 34th international conference on machine learning-volume 70*, JMLR. Org; 2017. p. 2979–87.
- [30] M. Abadi, A. Agarwal, P. Barham, E. Brevdo, Z. Chen, C. Citro, G. S. Corrado, A. Davis, J. Dean, M. Devin, et al., Tensorflow: large-scale machine learning on heterogeneous distributed systems, arXiv preprint arXiv:1603.04467.
- [31] Zeiler MD, Fergus R. Visualizing and understanding convolutional networks. In: *European conference on computer vision*, Springer; 2014. p. 818–33.
- [32] J. Yosinski, J. Clune, A. Nguyen, T. Fuchs, H. Lipson, Understanding neural networks through deep visualization, arXiv preprint arXiv:1506.06579.
- [33] E. Tjøa, C. Guan, A survey on explainable artificial intelligence (xai): towards medical xai, arXiv preprint arXiv:1907.07374.
- [34] Miorelli R, Kulakovskiy A, Chapuis B, Mesnil O, D'Almeida O, et al. Supervised learning strategy for classification and regression tasks applied to aeronautical structural health monitoring problems. *Ultrasonics* 2021;113:106372. <https://doi.org/10.1016/j.ultras.2021.106372>. In press.
- [35] Kulakovskiy A, Mesnil O, Chapuis B, d'Almeida O, Lhémy A. Statistical analysis of guided wave imaging algorithms performance illustrated by a simple structural health monitoring configuration. *J. Nondestr. Eval. Diagn. Prognostics Eng. Syst.* 2021;4:1–10. <https://doi.org/10.1115/1.4049571>. 031001 In press.